Exciton coherence length fluctuations in chromophore aggregates probed by multidimensional optical spectroscopy

František Šanda,[1,a)] Václav Perlík,[1] and Shaul Mukamel[2,b)]
[1]*Faculty of Mathematics and Physics, Institute of Physics, Charles University, Ke Karlovu 5, Prague 121 16, Czech Republic*
[2]*Department of Chemistry, University of California, Irvine, California 92697-2025, USA*

(Received 27 December 2009; accepted 10 May 2010; published online 2 July 2010)

The coherent third order optical response of molecular aggregates with fluctuating frequencies, couplings, and transition dipole moments is studied. We derived stochastic nonlinear exciton equations (SNEEs) by combining the quasiparticle picture of excitons with the path integral over stochastic bath paths described by the stochastic Liouville equations. Coherent two-dimensional (2D) spectra are calculated for a tetramer model system whose transition dipole orientations undergo two-state stochastic jumps on an arbitrary timescale. Correspondence between domains of ordered dipoles, which determine the exciton coherence length and the absorption peaks, is established. Signatures of domain coherence length fluctuations are observed in the cross peak dynamics of the 2D spectra in specific pulse polarization configurations. © *2010 American Institute of Physics*. [doi:10.1063/1.3442415]

I. INTRODUCTION

The modeling of the coherent nonlinear optical response of excitonic aggregates in fluctuating environments is a challenging task that has been addressed at various levels of theory.[1–6] A realistic description must include fluctuating transition frequencies, transition dipole moments, and dephasing rates, as well as exciton transport on arbitrary timescales. Developing numerically efficient approximation schemes is essential for applications to complex biological and chemical systems.

Current simulation approaches for electronic excitations of aggregates can be broadly sorted into two classes, which treat aggregates either as supermolecules or quasiparticles.[2] The supermolecule approach dissects the response to contributions from various Liouville space pathways (LSP) of the global (many-chromophore) states. The time evolution within each excitonic manifold (single exciton, two-exciton, etc.) is calculated separately by solving the Liouville equation. Diagonal Gaussian fluctuations can be conveniently incorporated by the cumulant expansion. The Redfield equations[7] describe exciton transport induced by fast (white noise) off-diagonal fluctuations. Collective bath coordinates can be used to describe broader classes of fluctuations.[8] However, any combination of cumulants and master equations treats on- and off-diagonal Hamiltonian fluctuations differently and refers to a fixed basis and thus does not describe slowly fluctuating eigenstates.

The stochastic Liouville equations (SLE)[9,10] and its finite temperature extensions[11–14] interpolate between regimes, where either Redfield equations hold (when each bath configuration is visited during one period of quantum coherence) or where static averaging is applicable. They may be thus used to describe slow off-diagonal fluctuations. SLE can describe any type of Markovian fluctuations (not only Gaussian profiles).

Stochastic dynamics is commonly used to describe spectral diffusion and hydrogen bonding of liquids.[15–20] The vibrational frequency varies when hydrogen bonds form or break. Hydrogen bonding is thus monitored by fluctuations of vibrational frequency, and its timescale can be conveniently deduced from the two-dimensional (2D) spectrum.[19–22] The monitored process itself is not manipulated by laser pulse, i.e., it is bath process that can be described by the SLE. This is, however, the simplest case, where only the transition frequency is modulated and the 2D spectrum directly probes profile and timescales of the bath path.[23]

More complex effects emerge when the exciton delocalization is modified by the bath. For instance, 2D spectra measure how the selection rules for excitation of two coupled (symmetric) levels are relaxed by slow spectral diffusion and otherwise dark level acquires transient dipole moment.[24] 2D spectra have also been instrumental in the study of conformation dynamics in peptides[25] through exciton fluctuations between coupled amide vibrations.

Destructive interference between various LSPs common in larger aggregates complicates the supermolecule approach due to large cancellations of similar contributions. The quasiparticle nonlinear exciton equations (NEE) approach[26,27] solves this problem. It simulates the observables directly and avoids the calculation of global eigenstates and the various LSP. Most current implementations of the NEE only include fast bath fluctuations by adding relaxation kernels disregarding the effect of the finite fluctuation timescale.

In this paper we generalize the NEE to include arbitrary timescale fluctuations. We include Markovian stochastic bath processes, over which the path integration is carried out ex-

a)Electronic mail: sanda@karlov.mff.cuni.cz.
b)Electronic mail: smukamel@uci.edu.

actly by the stochastic NEEs (SNEEs). In principle, the SNEE is equivalent to the SLE (Langevin versus master equation description of the same physical process). However, the two differ in computational cost and numerical accuracy and suggest different approximation schemes. The SNEE shares the numerical advantages of quasiparticle approach, as it eliminates the large cancellations between various LSPs of the supermolecule approach. We then apply the SNEE to model the dynamics of exciton delocalization induced by changing chromophore orientations within the molecular aggregate. Intermolecular coupling between molecules with parallel transition dipoles delocalizes the eigenstates. Perpendicular dipoles, in contrast, do not couple and localize the states. Local fields which shift site frequencies during orientation flips also localize the state. Regions of ordered and disordered dipoles may be identified in the spectra. We will demonstrate that 2D photon echo spectra monitor the transformation of structural motifs by orientation jumps. We will also show how the SNEE connects the molecule orientation dynamics with the dynamics of optical coherence and properly account for variations of the time-dependent coherence length.

We focus on discrete fluctuations (jumps) as recently observed in liquids[28–31] or photosynthetic aggregates.[32,33] In the two-state model of orientation jumps, which affect transition dipole moment and modify molecular frequencies and intermolecular (dipole-dipole) couplings, the coherence length can be easily defined by the ordered region, and signatures of its variations are predicted in the 2D photon echo spectrum.

II. THE SNEE FOR INTERACTING BOSONS

We first derive the SNEE in general form using the quasiparticle representation for the stochastic quantum dynamics. To that end we consider a system of boson modes with pairwise interactions described by the stochastic Hamiltonian

$$\hat{H} = \hbar \sum_{mn} h_{mn;\{q\}} \hat{b}_m^\dagger \hat{b}_n + \frac{\hbar}{2} \sum_{mnm'n'} V_{mn,m'n';\{q\}} \hat{b}_m^\dagger \hat{b}_n^\dagger \hat{b}_{m'} \hat{b}_{n'}, \tag{1}$$

where $\hat{b}_m^\dagger$ and $\hat{b}_m$ are creation and annihilation bosonic operators and h_{mn} and $V_{mn,m'n'}$ are matrix elements of one-particle Hamiltonian and two particle interaction, respectively. Both h_{mn} and $V_{mn,m'n'}$ coefficients depend on a set of stochastic bath coordinates $\{q\}$ whose time evolution $\{q\}(t)$ causes fluctuations of Hamiltonian [Eq. (1)]. Interaction with the sequence of probing laser pulses assumes dipole form. Next we assume that distance between bosons is much shorter than wavelength and all coupled bosons can be considered at the same macroscopic location $\vec{r}$. Interaction Hamiltonian in the rotating wave approximation is given by

$$\hat{H}'(t) = \hbar \sum_m (\mu^-_{m;\{q\}}(t) \hat{b}_m^\dagger + \mu^+_{m;\{q\}}(t) \hat{b}_m),$$

$$\mu^-_{m;\{q\}}(t) \equiv -\frac{1}{\hbar} \sum_j \vec{\boldsymbol{\mu}}_{m;\{q\}} \cdot \vec{E}_j f(t-\tau_j) e^{i\vec{\mathbf{k}}_j \cdot \vec{r} - i\omega_j t}, \tag{2}$$

$$\mu^+_{m;\{q\}}(t) = [\mu^-_{m;\{q\}}(t)]^*.$$

Here $\vec{\boldsymbol{\mu}}_{m;\{q\}} = (\boldsymbol{\mu}^x_{m;\{q\}}, \boldsymbol{\mu}^y_{m;\{q\}}, \boldsymbol{\mu}^z_{m;\{q\}})$ is the transition dipole moment of mth boson (matrix element between the ground and excited state), $\vec{E}_j = (E_j^x, E_j^y, E_j^z)$ is the polarization vector of the jth laser pulse with wavevector $\vec{\mathbf{k}}_j$ and envelope $f(t)$ reaching the system at times τ_j, and the asterisk * stands for complex conjugate.

The process $\{q\}(t)$ modulates the Hamiltonian parameters [Eq. (1)]. We assume that $\{q\}(t)$ is a Markovian stochastic process[34] whose density $P(\{q\})$ satisfies a master equation

$$\frac{dP(\{q\})}{dt} = \sum_{\{q'\}} T_{\{q\}\{q'\}} P(\{q'\}). \tag{3}$$

The off-diagonal elements of the matrix $T_{\{q\}\{q'\}}$ are rates for jumps from bath configuration $\{q'\}$ to $\{q\}$. The elements on diagonal satisfy $T_{\{q'\}\{q'\}} = -\Sigma_{\{q\}\neq\{q'\}} T_{\{q\}\{q'\}}$, which ensures the conservation of total density $\Sigma_{\{q\}} P(\{q\}) = 1$.

Fluctuations in the Hamiltonian can be incorporated into the quantum dynamics by direct generation of stochastic paths $\{q\}(t)$ (see, e.g., Ref. 16 for application to vibrational lineshapes of water). An alternative approach, which has been applied for nonlinear spectroscopy of molecules and small aggregates,[24,25,35] allows for analytical integration over bath paths by using SLEs [Eq. (A1)]. The SNEE is obtained by combining it with the calculation strategy used to derive quasiparticle NEEs.[2,26]

We introduce the (bosonic) density matrix $\hat{\rho}_{\{q\}}(t) \equiv \{\hat{\rho}(t) | \{q\}(t) = \{q\}\}$ in a given bath state $\{q\}$, normalized to $\mathrm{Tr}\, \hat{\rho}_{\{q\}} = P(\{q\})$ (i.e., the normal bosonic density matrix $\hat{\rho} = \Sigma_{\{q\}} \hat{\rho}_{\{q\}}$). Convenient simulation strategy will be based on averages $\langle \ldots \rangle_{\{q\}} \equiv \mathrm{Tr} \ldots \hat{\rho}_{\{q\}}$. Equations of motion for the quantities $\langle \hat{b}_m \rangle_{\{q\}} \equiv \mathrm{Tr}[\hat{b}_m \hat{\rho}_{\{q\}}]$, $\langle \hat{b}_m \hat{b}_n \rangle_{\{q\}} \equiv \mathrm{Tr}[\hat{b}_m \hat{b}_n \hat{\rho}_{\{q\}}]$, $\langle \hat{b}_m^\dagger \hat{b}_n \rangle_{\{q\}} \equiv \mathrm{Tr}[\hat{b}_m^\dagger \hat{b}_n \hat{\rho}_{\{q\}}]$, and $\langle \hat{b}_k^\dagger \hat{b}_m \hat{b}_n \rangle_{\{q\}} \equiv \mathrm{Tr}[\hat{b}_k^\dagger \hat{b}_m \hat{b}_n \hat{\rho}_{\{q\}}]$ are derived in Appendix A. Two methods are presented based on either SLEs or direct path integration of the NEEs. The resulting *SNEE* truncated to represent the third order response reads

$$i \frac{d}{dt} \langle \hat{b}_m \rangle_{\{q\}} = \sum_{m'} h_{mm';\{q\}} \langle \hat{b}_{m'} \rangle_{\{q\}} + \sum_{m'kl} V_{mm',kl;\{q\}} \langle \hat{b}_{m'}^\dagger \hat{b}_k \hat{b}_l \rangle_{\{q\}} + i \sum_{\{q'\}} T_{\{q\}\{q'\}} \langle \hat{b}_m \rangle_{\{q'\}} + \mu^-_{m;\{q\}} P(\{q\}), \tag{4}$$

$$i \frac{d}{dt} \langle \hat{b}_m \hat{b}_n \rangle_{\{q\}} = \sum_{m'n'} h^{(Y)}_{mn,m'n';\{q\}} \langle \hat{b}_{m'} \hat{b}_{n'} \rangle_{\{q\}} + i \sum_{\{q'\}} T_{\{q\}\{q'\}} \langle \hat{b}_m \hat{b}_n \rangle_{\{q'\}} + \mu^-_{m;\{q\}} \langle \hat{b}_n \rangle_{\{q\}} + \mu^-_{n;\{q\}} \langle \hat{b}_m \rangle_{\{q\}}, \tag{5}$$

$$i\frac{d}{dt}\langle \hat{b}_m^\dagger \hat{b}_n\rangle_{\{q\}} = \sum_k [h_{nk;\{q\}}\langle \hat{b}_m^\dagger \hat{b}_k\rangle_{\{q\}} - h_{km;\{q\}}\langle \hat{b}_k^\dagger \hat{b}_n\rangle_{\{q\}}] + i\sum_{\{q'\}} T_{\{q\}\{q'\}}\langle \hat{b}_m^\dagger \hat{b}_n\rangle_{\{q'\}} - \mu^+_{m;\{q\}}\langle \hat{b}_n\rangle_{\{q\}} + \mu^-_{n;\{q\}}\langle \hat{b}_m^\dagger\rangle_{\{q\}}, \quad (6)$$

$$i\frac{d}{dt}\langle \hat{b}_k^\dagger \hat{b}_m \hat{b}_n\rangle_{\{q\}} = \sum_{m'n'} h^{(Y)}_{mn,m'n';\{q\}}\langle \hat{b}_k^\dagger \hat{b}_{m'}\hat{b}_{n'}\rangle_{\{q\}} - \sum_{k'} h_{k'k;\{q\}} \times \langle \hat{b}_{k'}^\dagger \hat{b}_m \hat{b}_n\rangle_{\{q\}} + i\sum_{\{q'\}} T_{\{q\}\{q'\}}\langle \hat{b}_k^\dagger \hat{b}_m \hat{b}_n\rangle_{\{q'\}} + \mu^-_{m;\{q\}}\langle \hat{b}_k^\dagger \hat{b}_n\rangle_{\{q\}} + \mu^-_{n;\{q\}}\langle \hat{b}_k^\dagger \hat{b}_m\rangle_{\{q\}} - \mu^+_{k;\{q\}}\langle \hat{b}_m \hat{b}_n\rangle_{\{q\}}, \quad (7)$$

where

$$h^{(Y)}_{mn,m'n';\{q\}} \equiv h_{mm';\{q\}}\delta_{nn'} + h_{nn';\{q\}}\delta_{mm'} + V_{mn,m'n';\{q\}} \quad (8)$$

is the Hamiltonian for the two exciton manifold. Averages $\langle \hat{b}_m\rangle_{\{q\}}$, $\langle \hat{b}_m\hat{b}_n\rangle_{\{q\}}$, $\langle \hat{b}_m^\dagger \hat{b}_n\rangle_{\{q\}}$, and $\langle \hat{b}_k^\dagger \hat{b}_m\hat{b}_n\rangle_{\{q\}}$, and Eqs. (4)–(7) depend parametrically on position $\vec{r}$, but only through simple phase factor of Eq. (2).

We define the Green's function $G_{m\{q\},m'\{q'\}}$ for the entire set of all boson m and bath $\{q\}$ states $\langle \hat{b}_m\rangle_{\{q\}}$ by the homogenous part of Eq. (4),

$$i\frac{d}{dt}G_{m\{q\},m'\{q'\}} = \sum_{m''} h_{mm'';\{q\}}G_{m''\{q\},m'\{q'\}} + i\sum_{\{q''\}} T_{\{q\}\{q''\}}G_{m\{q''\},m'\{q'\}} + i\delta_{mm'}\delta_{\{q\}\{q'\}}\delta(t). \quad (9)$$

The Green's functions for $\langle \hat{b}_m\hat{b}_n\rangle_{\{q\}}$ [Eq. (5)], $\langle \hat{b}_m^\dagger \hat{b}_n\rangle_{\{q\}}$ [Eq. (6)], and $\langle \hat{b}_k^\dagger \hat{b}_m\hat{b}_n\rangle_{\{q\}}$ [Eq. (7)] can be similarly derived for homogenous part of the respective SNEE and will be denoted as $\mathcal{G}_{mn\{q\},m'n'\{q'\}}$, $\mathcal{G}^{(N)}_{mn\{q\},m'n'\{q'\}}$, and $\mathcal{G}^{(Z)}_{kmn\{q\},k'm'n'\{q'\}}$, respectively. Note that all the Greens functions are independent on $\vec{r}$. The microscopic polarization generated by a single bosonic system is calculated by expanding the polarization vector $\vec{\mathbf{P}}_{\{q\}} \equiv \Sigma_m \vec{\boldsymbol{\mu}}^*_{m;\{q\}}\langle \hat{b}_m\rangle_{\{q\}} + \text{c.c.}$ perturbatively in electric field and averaged over bath paths $\langle \ldots\rangle = \text{Tr}\ldots\hat{\rho} = \Sigma_{\{q\}}\langle \ldots\rangle_{\{q\}}$.

The 2D experiments are carried on macroscopic samples much larger than wavelength and made of uniformly distributed identical systems of Eq. (1). The outgoing signal is proportional to the Fourier components of the polarization $S^a_{\vec{\mathbf{k}}}(t) = (2\pi)^{-3}\int d^3 r e^{-i\vec{\mathbf{k}}\cdot\vec{r}}\Sigma_{\{q\}}\mathbf{P}^a_{\{q\}}(t,\vec{r})$. Phase factors of Eq. (2) limit the signal to one of the phase matching directions $\vec{\mathbf{k}}_{\text{out}} = \Sigma_j \pm \vec{\mathbf{k}}_{\mathbf{j}}$.

The linear signal generated by short $(f(t)=\delta(t))$ pulse E^b_1 is described by linear response functions $I^{ab}(t)$,

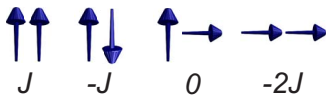

FIG. 1. Dipole-dipole intermolecular coupling [Eq. (25), $J \equiv \mu^2/d^3_{mn}$] for various configurations of transition dipole moments.

$$S^a_{\vec{\mathbf{k}}}(t) = \delta(\vec{\mathbf{k}} - \vec{\mathbf{k}}_1)\sum_b I^{ab}(t)E^b + \delta(\vec{\mathbf{k}} + \vec{\mathbf{k}}_1)\sum_b I^{ab*}(t)E^b. \quad (10)$$

Imaginary part of its Fourier transform $I^{ab}(\Omega) = \int_0^\infty I^{ab}(t)e^{i\Omega t}dt$ corresponds to the absorption spectrum. By solving Eq. (4) we get

$$I^{ab}(\Omega) = \frac{i}{\hbar}\sum_{m_1,m_2}\sum_{\{q^\alpha\},\{q^\beta\}} \boldsymbol{\mu}^{a*}_{m_2;\{q^\beta\}}\boldsymbol{\mu}^{b}_{m_1;\{q^\alpha\}}G_{m_2\{q^\beta\},m_1\{q^\alpha\}}(\Omega) \times P(\{q^\alpha\}). \quad (11)$$

The polarization $\mathbf{P}^a(t_1+t_2+t_3)$ generated by three short pulses E^d_1, E^c_2, and E^b_3 at times 0, t_1, and t_1+t_2 is described by the third order response function $R^{abcd}(t_3,t_2,t_1)$. The photon echo signal generated in the $\vec{\mathbf{k}}_1 = -\vec{\mathbf{k}}_1 + \vec{\mathbf{k}}_2 + \vec{\mathbf{k}}_3$ direction is calculated in Appendix B by solving Eqs. (4)–(7) to third order in the electric field by direct extension of the results in Ref. 2. The response function in the frequency domain [Eq. (B3)] reads

$$R^{abcd}_{\mathbf{k}_1}(\Omega_3,\Omega_2,\Omega_1) = 2i\sum_{m_{1-4}m'_{1-4}m''_{1-2}m'''_1}\sum_{q^{\alpha-\eta}}\left(\frac{i}{\hbar}\right)^3 \boldsymbol{\mu}^{a*}_{m_4;\{q^\delta\}}\boldsymbol{\mu}^{b}_{m_3;\{q^\gamma\}} \times \boldsymbol{\mu}^{c}_{m_2;\{q^\beta\}}\boldsymbol{\mu}^{d*}_{m_1;\{q^\alpha\}}G_{m_4\{q^\delta\}m'_4\{q^\eta\}}(\Omega_3) \times V_{m'_4m'_1,m'_3m'_2;\{q^\eta\}}\mathcal{G}^{(Z)}_{m'_1m'_3m'_2\{q^\eta\},m''_1m_3m''_2\{q^\gamma\}}(\Omega_3) \times \mathcal{G}^{(N)}_{m''_1m''_2\{q^\gamma\},m'''_1m_2\{q^\beta\}}(\Omega_2)G^*_{m'''_1\{q^\beta\},m_1\{q^\alpha\}}(-\Omega_1)P(\{q^\alpha\}). \quad (12)$$

where $\Omega_1,\Omega_2,\Omega_3$ are Fourier conjugated to t_1,t_2,t_3 [Eq. (B3)]. The other third order signals are given in Appendix B.

III. EXCITON HAMILTONIAN OF AGGREGATES WITH FLUCTUATING CHROMOPHORE ORIENTATIONS

We now apply the SNEE to optical properties of molecular aggregates. A linear chain of N molecules with nearest neighbor coupling is described by the Frenkel exciton Hamiltonian[36–38]

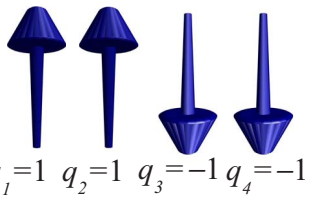

FIG. 2. Sample configuration *uudd* of model in Sec. III A.

$$H_F = \hbar \sum_{m=1}^{N} \varepsilon_m(t) \hat{B}_m^\dagger \hat{B}_m + \hbar \sum_{m=1}^{N-1} J_{mm+1}(t) \hat{B}_m^\dagger \hat{B}_{m+1} + J_{m+1m}(t) \hat{B}_{m+1}^\dagger \hat{B}_m, \quad (13)$$

where ε_m are exciton frequencies and $\hbar J_{mn}$ is intermolecular coupling. Electronic excitations are not bosons, and the double excitations of the same molecule are strongly shifted from the single excitation frequencies. For two level chromophores exciton creation (annihilation) operators $\hat{B}_m^\dagger, (\hat{B}_m)$ obey the Pauli commutation rule $[\hat{B}_m, \hat{B}_n^\dagger] = \delta_{m,n}(1 - 2\hat{B}_n^\dagger \hat{B}_m)$.

To connect with the boson formalism of the previous section, we formally allow double excitations to reside on the same molecule but add a energy penalty (anharmonicity)

$$V_{mn,m'n';\{q\}} = \Delta_m \delta_{mm'} \delta_{mn} \delta_{nn'}. \quad (14)$$

The third order response can be then calculated by using the SNEE [Eq. (4)–(7)], with one-particle Hamiltonian

$$h_{mn;\{q\}} = \varepsilon_{m;\{q\}} \delta_{mn} + J_{mm+1;\{q\}}(\delta_{mn+1} + \delta_{m+1n}), \quad (15)$$

and two-particle interaction Eq. (14) in $\Delta_m \to \infty$ limit, which exclude the double excitation from the spectrum and account for the Pauli exclusion.

In other words, creation and annihilation operators in exciton Hamiltonian have to be changed to the bosonic one $\hat{B}_m \to \hat{b}_m$, $\hat{B}_m^\dagger \to \hat{b}_m^\dagger$ with certain adjustment of two-particle interaction. Bosonization procedure required for higher (>3) response functions is summarized in Ref. 2. Bosonization schemes for general types of excitons are also well developed.[39]

In practical simulations, we took Δ_m to be finite and large. The doubly excited state must be represented in practical implementation of the SNEE [Eqs. (4)–(7)], and the $\Delta_m \to \infty$ limit has to be taken at the end of calculation.

We shall investigate signatures of molecular reorientation in the linear and third order optical spectra. We assume that mth molecule randomly jumps between two orientations associated to two states of local bath coordinate $q_m = 1$ (we will call it u-state) and $q_m = -1$ (d-state). The complete bath configuration is a collection $\{q\} \equiv \{q_1, q_2, \ldots, q_N\}$.

We next assume that molecules jump independently. This neglects interaction between permanent dipoles in the electronic ground state $|g\rangle$ (defined by $\hat{B}_m|g\rangle = 0$). Dynamics then satisfies local master equations

$$\frac{dP_m(q_m)}{dt} = \sum_{q_m'=1,-1} \tilde{T}^{(m)}_{q_m q_m'} P_m(q_m'). \quad (16)$$

Markovian master equation [Eq. (3)] for the whole process $\{q\}(t)$ is then obtained by combining jumps rates $\tilde{T}^m$ of Eq. (16),

$$T_{\{q\}\{q'\}} = \sum_{m=1}^{N} \tilde{T}^{(m)}_{q_m q_m'}. \quad (17)$$

We limit simulations to high temperatures with equal rates k for all molecules and both $u \to d$ and $d \to u$ bath jumps

$$\tilde{T}^{(m)}_{q_m q_m'} = \begin{pmatrix} -k & k \\ k & -k \end{pmatrix}. \quad (18)$$

The transition dipole moment between the ground and the excited state of the mth molecule [enters the model in Eq. (2)] is a vector function $\vec{\boldsymbol{\mu}}_{m;\{q\}} \equiv \vec{\boldsymbol{\mu}}_m(q_m)$. The Hamiltonian parameters ε and J [of Eq. (13)] also depend on the bath configuration $\{q\} = \{q_1, \ldots, q_N\}$. Transition frequencies ε_m are shifted by local field $\vec{\mathcal{E}}$,

$$\varepsilon_{m;\{q\}} = \bar{\varepsilon} + \vec{\mathcal{E}} \cdot \vec{\boldsymbol{\mu}}_m(q_m).$$

The intermolecular coupling has dipole-dipole form

$$J_{mn;\{q\}} = \frac{1}{4\pi\epsilon} \left\{ \frac{\vec{\boldsymbol{\mu}}_m(q_m) \cdot \vec{\boldsymbol{\mu}}_n(q_n)}{d_{mn}^3} - 3\frac{(\vec{\boldsymbol{\mu}}_m(q_m) \cdot \vec{d}_{mn})(\vec{\boldsymbol{\mu}}_n(q_n) \cdot \vec{d}_{mn})}{d_{mn}^5} \right\}, \quad (19)$$

where d_{mn} are the intermolecular distances and ϵ is permittivity. The exciton coupling falls rapidly $J_{mn} \sim 1/|m-n|^3$ with distance, and it will be approximated by nearest neighbor interaction [Eq. (13)]. Figure 1 summarizes coupling between chromophores of various orientations.

In the next two subsections, we treat the effect of orientation jumps on collective dynamics of excitation coherence. In each subsection we discuss distinct mechanism, by which orientation jumps reduce the coherence length. The spectral diffusion during flips reduces the coherent length when the energy fluctuations are larger than coupling strength (weak coupling limit). This mechanism is treated for molecules that undergo flips in Sec. III A.

Delocalization is also absent when transition dipoles are perpendicular and the coupling vanishes (see Fig. 1). Jumps between transversal and perpendicular orientation of molecules will be examined in Sec. III B.

A. Linear tetramer with transition dipole moments perpendicular to its axis

We assume transition dipole moments with fixed magnitude μ whose orientations can flip between $\vec{\boldsymbol{\mu}}_m = (\mu, 0, 0)$ for u-state ($q_m = 1$) and $\vec{\boldsymbol{\mu}}_m = (-\mu, 0, 0)$ for d-state ($q_m = -1$) both perpendicular to the aggregate axis $\vec{d}_{mn} = D_0(0, m-n, 0)$, where D_0 is the distance between two molecules (see Fig. 2 for sample configuration). The molecular frequencies are

$$\varepsilon_{m;\{q\}} = \bar{\varepsilon} + \mu \mathcal{E}^x q_m. \quad (20)$$

We will set $\bar{\varepsilon} = 0$ and denote $\varepsilon \equiv \mu \mathcal{E}^x$ so that

$$\varepsilon_{m;\{q\}} = \varepsilon q_m \quad (21)$$

The intermolecular nearest neighbor coupling [Eq. (19)] is given by

$$J_{mn;\{q\}} = q_m q_n J \delta_{mn\pm 1}, \quad (22)$$

where we denoted $J \equiv \mu^2/(4\pi\epsilon D_0^3)$.

The coupling to the optical field is described by interaction Hamiltonian

TABLE I. Spectral analysis of the one-particle Hamiltonian [Eq. (15)] of a tetramer (Fig. 2). For each bath configuration (first column), eigenfrequencies E are given as a function of J,ε. Solutions (Ferrari–Cardano quartic formula) for characteristic equation $0=J^4-3J^2E^2+E^4+2J^2E\varepsilon+[J^2-2E^2]\varepsilon^2+\varepsilon^4$ of *uddd* configuration and characteristic equation $0=J^4-3J^2E^2+E^4+2(J^2-E^2)E\varepsilon+J^2\varepsilon^2+2E\varepsilon^3-\varepsilon^4$ of *uuud* configuration are complicated; we designate them by I–IV. Peaks in weak-coupling absorption spectra (Fig. 3) are assigned in the third column along with oscillator strength $\mathrm{u}^2\equiv(1/\mu)^2|\langle g|\Sigma_i\tilde{\boldsymbol{\mu}}_i^*(\{q\})\hat{B}_i|E\rangle|^2$ in the fourth column. Peaks of strong coupling absorption spectrum (bottom panels of Fig. 6) are assigned in the fifth column. Numerical values of E and u^2 for intermediate coupling (top panels of Fig. 6) are given oscillator strength in the sixth and last columns, respectively.

$\{q\}$	Exciton frequency E	$J\ll\varepsilon$	$\mathrm{u}^2_{J\ll\varepsilon}$	$J\gg\varepsilon$	$E_{J=\varepsilon}$	$\mathrm{u}^2_{J=\varepsilon}$
uuuu	$-\frac{1}{2}(\sqrt{5}+1)J+\varepsilon$	∅	0.00	∅	−0.62	0.00
	$\frac{1}{2}(-\sqrt{5}+1)J+\varepsilon$	$D_W{}'$	0.21	E	0.38	0.21
	$\frac{1}{2}(\sqrt{5}-1)J+\varepsilon$	∅	0	∅	1.62	0.00
	$\frac{1}{2}(\sqrt{5}+1)J+\varepsilon$	D′	3.79	F	2.62	3.79
uudu	$\frac{1}{2}(\varepsilon-\sqrt{J^2+\varepsilon^2}-\sqrt{5J^2+2\varepsilon^2+2\varepsilon\sqrt{J^2+\varepsilon^2}})$	A_2	0.96	∅	−1.77	0.11
	$\frac{1}{2}(\varepsilon-\sqrt{J^2+\varepsilon^2}+\sqrt{5J^2+2\varepsilon^2+2\varepsilon\sqrt{J^2+\varepsilon^2}})$	A_3'	0.99	∅	1.36	0.48
	$\frac{1}{2}(\varepsilon+\sqrt{J^2+\varepsilon^2}-\sqrt{5J^2+2\varepsilon^2-2\varepsilon\sqrt{J^2+\varepsilon^2}})$	∅	0.00	E	0.19	0.04
	$\frac{1}{2}(\varepsilon+\sqrt{J^2+\varepsilon^2}+\sqrt{5J^2+2\varepsilon^2-2\varepsilon\sqrt{J^2+\varepsilon^2}})$	B′	2.04	F	2.23	3.38
uudd	$-\sqrt{\varepsilon^2+\frac{1}{2}J(3J-\sqrt{5J^2+16\varepsilon^2})}$	B	1.98	E	−0.46	0.26
	$\sqrt{\varepsilon^2+\frac{1}{2}J(3J-\sqrt{5J^2+16\varepsilon^2})}$	∅	0.00	∅	0.46	0.86
	$-\sqrt{\varepsilon^2+\frac{1}{2}J(3J+\sqrt{5J^2+16\varepsilon^2})}$	∅	0.00	∅	−2.19	0.00
	$\sqrt{\varepsilon^2+\frac{1}{2}J(3J+\sqrt{5J^2+16\varepsilon^2})}$	B′	2.02	F	2.19	2.87
uduu	See *uudu*					
udud	$-\sqrt{\frac{1}{2}(3+\sqrt{5})J^2+\varepsilon^2}$	A_1	1.83	∅	−1.90	0.28
	$\sqrt{\frac{1}{2}(3+\sqrt{5})J^2+\varepsilon^2}$	A_1'	1.96	F	1.90	3.51
	$-\sqrt{-\frac{1}{2}(-3+\sqrt{5})J^2+\varepsilon^2}$	A_3	0.11	E	−1.18	0.16
	$\sqrt{-\frac{1}{2}(-3+\sqrt{5})J^2+\varepsilon^2}$	A_3'	0.10	∅	1.18	0.05
uddu	$\frac{1}{2}(J-\sqrt{5J^2-4J\varepsilon+4\varepsilon^2})$	B	1.96	E	−0.62	0.21
	$\frac{1}{2}(J+\sqrt{5J^2-4J\varepsilon+4\varepsilon^2})$	A_3'	2.04	F	1.62	3.79
	$\frac{1}{2}(-J-\sqrt{5J^2+4J\varepsilon+4\varepsilon^2})$	∅	0.00	∅	−2.30	0.00
	$\frac{1}{2}(-J+\sqrt{5J^2+4J\varepsilon+4\varepsilon^2})$	∅	0.00	∅	1.30	0.00
uddd	I	C_W	0.08	∅	−1.22	0.03
	II	∅	0.00	E	0.22	1.40
	III	C	2.89	∅	−2.50	0.03
	IV	A_3'	1.02	F	1.50	2.55
uuud	I	A_3	0.98	∅	−1.50	0.32
	II	$C_W{}'$	0.09	E	−0.22	0.26
	III	∅	0.00	∅	1.22	0.01
	IV	C′	2.93	F	2.50	3.41
dddd	$-\frac{1}{2}(\sqrt{5}+1)J-\varepsilon$	∅	0.00	∅	−2.62	0.00
	$\frac{1}{2}(-\sqrt{5}+1)J-\varepsilon$	D_W	0.21	E	−1.62	0.21
	$\frac{1}{2}(\sqrt{5}-1)J-\varepsilon$	∅	0.00	∅	−0.38	0.00
	$\frac{1}{2}(\sqrt{5}+1)J-\varepsilon$	D	3.79	F	0.62	3.79
ddud	$\frac{1}{2}(-\varepsilon-\sqrt{J^2+\varepsilon^2}-\sqrt{5J^2+2\varepsilon^2-2\varepsilon\sqrt{J^2+\varepsilon^2}})$	∅	0.00	∅	−2.23	0.01
	$\frac{1}{2}(-\varepsilon-\sqrt{J^2+\varepsilon^2}+\sqrt{5J^2+2\varepsilon^2-2\varepsilon\sqrt{J^2+\varepsilon^2}})$	B	1.96	∅	−0.19	0.58
	$\frac{1}{2}(-\varepsilon+\sqrt{J^2+\varepsilon^2}-\sqrt{5J^2+2\varepsilon^2+2\varepsilon\sqrt{J^2+\varepsilon^2}})$	A_3	1.00	E	−1.36	0.62
	$\frac{1}{2}(-\varepsilon+\sqrt{J^2+\varepsilon^2}+\sqrt{5J^2+2\varepsilon^2+2\varepsilon\sqrt{J^2+\varepsilon^2}})$	A_2'	1.04	F	1.78	2.80
dduu	See *uudd*					
dudd	See *ddud*					
dudu	See *udud*					
duud	$\frac{1}{2}(-J-\sqrt{5J^2-4J\varepsilon+4\varepsilon^2})$	∅	0.00	∅	−1.62	0.00
	$\frac{1}{2}(-J+\sqrt{5J^2-4J\varepsilon+4\varepsilon^2})$	∅	0.00	∅	0.62	0.00
	$\frac{1}{2}(J-\sqrt{5J^2+4J\varepsilon+4\varepsilon^2})$	A_3	1.96	E	−1.30	0.89
	$\frac{1}{2}(J+\sqrt{5J^2+4J\varepsilon+4\varepsilon^2})$	B′	2.04	F	2.30	3.11
dddu	See *uddd*					
duuu	See *uuud*					

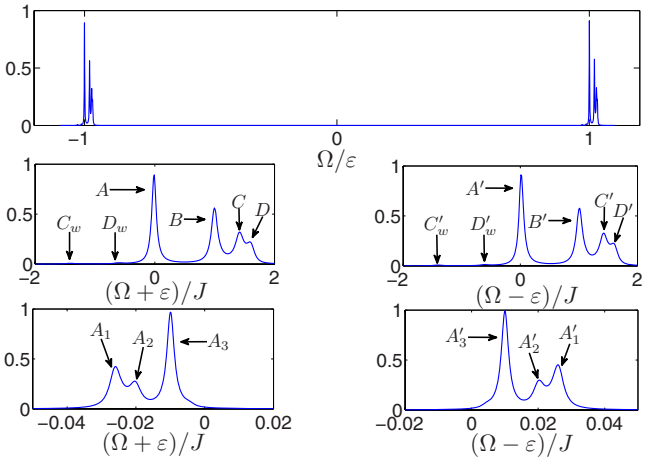

FIG. 3. Absorption spectra [Im I(Ω)] of weakly coupled $J/\varepsilon=0.02$ tetramer [Eqs. (11), (21), and (22)] in the slow bath limit $k/J=0.02$. Top: two groups of peaks are formed around $\Omega=-\varepsilon$ and $\Omega=\varepsilon$. Central: fine peak structure around $\Omega=-\varepsilon$ (left) and around $\Omega=\varepsilon$ (right) is shown on an expanded scale. Peaks A–D (A′–D′) are absorption of clusters of one to four *d*-states (*u*-states). Bottom: peak A on an expanded scale is further structured for very slow bath $k/J=0.0005 \ll J/\varepsilon=0.02$.

$$\hat{H}'_{\{q\}} = -\sum_{m=1}^{N}\sum_{j=1}^{3}\Big\{\mu q_m \hat{B}_m^\dagger E_j^x f(t-\tau_j)e^{i\vec{\mathbf{k}}_j\cdot\vec{r}-i\omega_j t} + \mu q_m \hat{B}_m E_j^x f(t-\tau_j)e^{-i\vec{\mathbf{k}}_j\cdot\vec{r}+i\omega_j t}\Big\}. \quad (23)$$

The optical response was calculated using Eqs. (11) and (12), after bosonization procedure Eqs. (14) and (15). We shall show the linear signal $I^{xx}(\Omega)$ and the imaginary part of photon echo signal $-\mathrm{Im}\, R^{xxxx}_{\mathbf{k}_\mathrm{I}}(\Omega_3,t_2,-\Omega_1)$. Sign convention ensures positive diagonal peaks at chromophore transition frequencies.

We first consider slow bath $k \ll \varepsilon, J$. For $k \to 0$ Green's function $G(\Omega)$ has poles at spectrum of one-particle Hamiltonian. Peak positions in absorption spectrum [Eq. (11)] are thus found by spectral analysis of $h_{mn,\{q\}}$ made in Table I.

The weak coupling $J \ll \varepsilon$ absorption spectrum shows two groups of peaks (Fig. 3). Molecules in *u* state absorb around $\Omega=\varepsilon$ and in *d* state absorb around $\Omega=-\varepsilon$. Fine structure (central panels) is caused by exciton delocalization between coupled molecules. Excitons can only be delocalized among molecules with similar frequencies. Peaks A–D thus correspond to the excitons delocalized over clusters of one (A) to four (D) neighboring molecules with the same orientation (one exciton always carries most oscillator strength in cluster). Peak position is obtained by diagonalizing Hamiltonian on the cluster (agree with Table I in $J/\varepsilon \to 0$ limit). Peak magnitudes are determined by an oscillator strength u^2 (Table I) and by the density of clusters *w* in the ensemble (Table II). Oscillator strength and coherence length are proportional to length of a cluster, which thus characterizes the structure.

As an example, we discuss the spectrum around $\Omega \approx -\varepsilon$ (central left panel of Fig. 3). Peak A at $\Delta\Omega \equiv \Omega+\varepsilon=0$ is assigned to *d* site surrounded by *u*-sites, with oscillator strength $\mathrm{u}^2=1$ and density factor $w=3/4$. Peak B at $\Delta\Omega=J$ is due to dimer (*dd*) cluster ($w=5/16, \mathrm{u}^2=2$). The other dimer eigenstate $\Delta\Omega=-J$ is dark ($\mathrm{u}^2=0$). Diagonalization of the *ddd* cluster Hamiltonian explains peak C ($w=1/8, \mathrm{u}^2=(3+\sqrt{2})/2$) at $\Delta\Omega=\sqrt{2}J$ and weak peak C_W ($\mathrm{u}^2=(3-\sqrt{2})/2$) at $\Delta\Omega=-\sqrt{2}J$. The remaining state $\Delta\Omega=0$ is dark. Finally, an all-parallel *dddd* cluster ($w=1/16$) yields peak D ($\mathrm{u}^2=2+4/\sqrt{5}$) at $\Delta\Omega=\frac{1}{2}(\sqrt{5}+1)J$ and small peak D_W ($\mathrm{u}^2=2-4/\sqrt{5}$) at $\Delta\Omega=\frac{1}{2}(-\sqrt{5}+1)J$. Other levels of *dddd* cluster $\Delta\Omega=\frac{1}{2}(\sqrt{5}-1)J$ and $\Delta\Omega=\frac{1}{2}(\sqrt{5}-1)J$ are dark. The $\Omega \approx \varepsilon$ peak is structured into features A′, B′, C′, and D′ (Fig. 3, bottom right), which are shifted from ε by the same values $\Delta\Omega$ as peaks A, B, C, D from $-\varepsilon$ and correspond to *u*, *uu*, *uuu*, and *uuuu* clusters.

TABLE II. Density of clusters *w* in aggregate at high temperatures. Combinatorial weight of all-parallel clusters in the chain with random *u* or *d* orientation of dipoles.

Polymer\cluster	*d*	*dd*	*ddd*	*dddd*	*ddddd*
Monomer	1/2				
Dimer	1/2	1/4			
Trimer	5/8	1/4	1/8		
Tetramer	3/4	5/16	1/8	1/16	
Pentamer	7/8	3/8	5/32	1/16	1/32

Peaks are further structured, as the eigenfrequencies also depend on the cluster surrounding. This structure may be resolved for narrow peaks satisfying the condition $k < J^2/\varepsilon$ (peak width *k* is compared with frequency splitting as found in Table I between, e.g., two eigenstates around $-\varepsilon$ of *udud* configuration). Peak A is split at Fig. 3, bottom panel, into three features A_1, A_2, and A_3 (A′ into A'_1, A'_2, and A'_3). Feature A_1 corresponds to case when *d* is surrounded by two monomers *u* (i.e., configuration $u\underline{d}ud$) (underlined chromophore is dominantly occupied), for A_2 is *d* surrounded by *u* monomer and *uu* dimers (configuration $uu\underline{d}u$). Finally A_3 feature covers all *d*-terminating configurations ($udu\underline{d}$, $uuu\underline{d}$, $ddu\underline{d}$, and $\underline{d}uu\underline{d}$).

The corresponding 2D spectra of photon echo signal [Eq. (12)] at zero delay time $t_2=0$ are shown in Fig. 4. We see eight major diagonal peaks corresponding to A, B, C, D, A′, B′, C′, and D′ in Fig. 3. Additional six off-diagonal negative-going features are poles of $\mathcal{G}^{(Z)}(\Omega_3)$ versus $G(\Omega_1)$ and correspond to excited state absorption. Peak $\mathcal{B}$ at

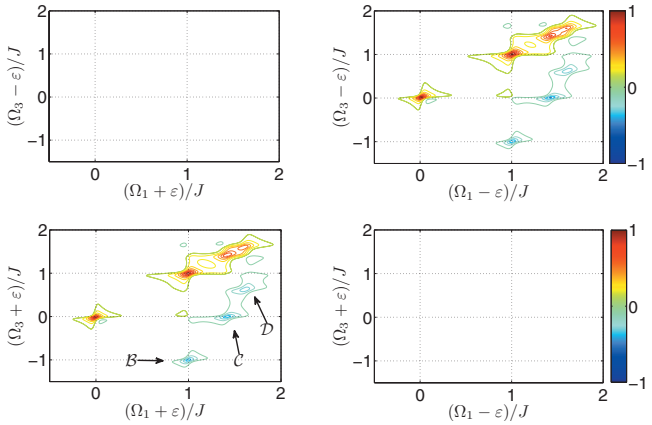

FIG. 4. The 2D photon echo $(-\mathrm{Im}\, R_{\mathbf{k}_\mathrm{I}}(\Omega_3,t_2=0,-\Omega_1))$ signal [Eq. (12)] from weakly coupled tetramer (parameters correspond to Fig. 3). Both diagonal $(\varepsilon,\varepsilon)$, $(-\varepsilon,-\varepsilon)$ and off-diagonal $(\varepsilon,-\varepsilon)$, $(-\varepsilon,\varepsilon)$ regions are shown.

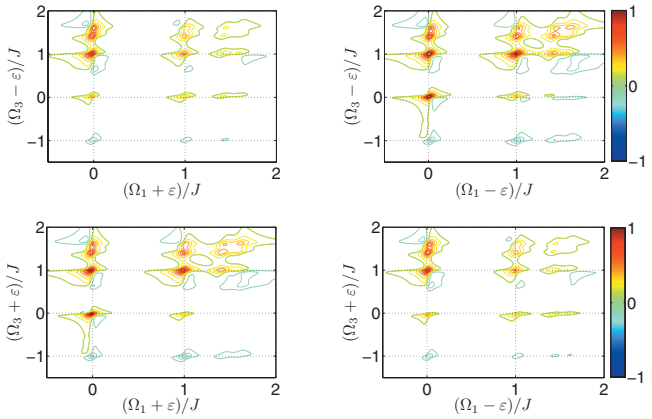

FIG. 5. Same as in Fig. 4 but for delay time $kt_2=1$.

$(\Omega_1,\Omega_3)=(-\varepsilon+J,-\varepsilon-J)$ comes from *dd* cluster: two exciton level $\hat{B}_1^\dagger\hat{B}_2^\dagger|g\rangle$ (frequency -2ε) of a symmetric dimer has a large transition dipole with the symmetric state of dimer $(\hat{B}_1^\dagger+\hat{B}_2^\dagger)|g\rangle$ (frequency $-\varepsilon+J$; pole of $\mathcal{G}^{(Z)}(\Omega_3)$ is thus at $-\epsilon-J$). Similarly, the *ddd* cluster induces peak $\mathcal{C}$ at $(\sqrt{2}J,0)$ and *dddd* cluster adds peak $\mathcal{D}$ at $([\sqrt{5}+1]J/2,[\sqrt{5}-1]J/2)$. Isolated chromophore cannot be doubly excited, so there is no similar peak related to *d* cluster.

At longer delay times $kt_2\sim 1$ the bath is reconfigured, and the cluster (coherence) length is changed. Figure 5 shows the evolution of the 2D spectrum of weakly coupled aggregate with delay time t_2. The cross peaks grow, and their volumes measure the rates of clusters transformation via bath-induced fluctuations. Dynamics of structural motifs is thus reflected in 2D correlation spectrum, e.g., $ddd\rightarrow dd$ transformation is found at B and C cross peaks.

For intermediate coupling strength $J\approx\varepsilon$, the two groups of peaks overlap and the pattern becomes rather complex (top panels of Fig. 6). The oscillator strength accumulates at larger $(\Omega>0)$ frequencies (see the sixth and seventh column of Table I). The 2D signal is dominated by a large structured diagonal peak between $J<\Omega<2J$. First $(t_2=0)$ it is rather elongated; loss of memory with t_2 gives the 2D lineshape more rounded shape.

The strong coupling $J\gg\varepsilon$ lineshape (bottom left panel of Fig. 6) has two peaks: at $\Omega=\frac{1}{2}(\sqrt{5}+1)J$, strong peak F

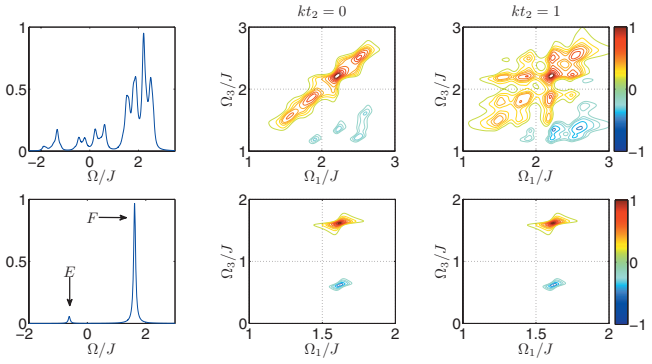

FIG. 6. Moderately coupled $J=\varepsilon$ (top panels) and strongly coupled $\varepsilon=0$ (bottom) tetramer in the slow bath limit $k/J=0.05$. From left: absorption spectrum [Im I(Ω) Eq. (11)], the 2D photon echo signal [$-\mathrm{Im}\,R_{\mathbf{k}_I}(\Omega_3,t_2,-\Omega_1)$, Eq. (12)] for delay times $t_2=0$ and $kt_2=1$.

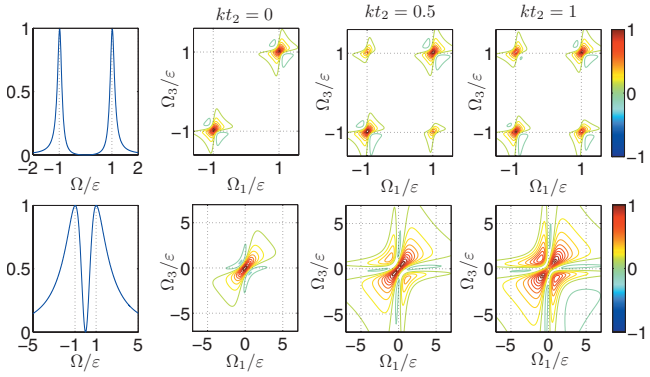

FIG. 7. Effect of bath timescale in absorption (left panel) and 2D spectrum $(-\mathrm{Im}\,R_{\mathbf{k}_I}(\Omega_3,t_2,-\Omega_1))$ at delay times (from left to right) $kt_2=0$, $kt_2=0.5$, $kt_2=1$, of weakly coupled $J/\varepsilon=0.02$ tetramer. Top: $k/\varepsilon=0.1$ Bottom: $k/\varepsilon=1$.

$(u^2=2+4/\sqrt{5})$ and at $\Omega=\frac{1}{2}(-\sqrt{5}+1)J$, much weaker peak E $(u^2=2-4/\sqrt{5})$. Peak assignment is given by the fifth column of Table I. Interestingly, the eigenfrequencies and associated oscillator strength (for aggregate of any size) are not affected by jumps. Contributions from all bath configurations $\{q\}$ are equal in $\varepsilon=0$ limit since the effect of flipping of q_mth bath state can be eliminated by unitary transformation $B_m\rightarrow -B_m$ and $B_m^\dagger\rightarrow -B_m^\dagger$. There is no link between structure and spectrum in the strong coupling limit; dipole flips cannot be observed. The 2D spectra are dominated by peak F; t_2 evolution does not carry much dynamical information. Peak E is weak and scales as u_E^4. Additional negative peak at $([\sqrt{5}+1]J/2,[\sqrt{5}-1]J/2)$ can be explained as in Fig. 4.

Stochastic quantum dynamics has been developed to interpolate between various bath timescale limits. We complete the discussion of model IIIA by studying how the weakly varying parameters are averaged by the fast bath. In top panels of Fig. 7, the peaks resolved by the energy splitting $\varepsilon/k\gg 1$ between *u* and *d* states remain separated, but the fine structure disappears from the spectrum when the coupling is averaged out $J/k\ll 1$ (Fig. 7). A simple two-state bath dynamics is observed with increasing delay time.

When the jump rates become comparable with energy splitting $(\varepsilon/k\approx 1)$, the peaks overlap due to motional narrowing (bottom panels of Fig. 7). Dip at the central frequency of absorption is always present, narrows down, but does not vanish even for fluctuations faster than any other timescale of the model $J/k\ll 1,\varepsilon/k\ll 1$. Vanishing average of the transition dipole moment stays behind this surprising behavior, which contrasts with Lorentzian peak of motional narrowing limit of the standard Kubo–Anderson spectral diffusion[40,41] with fixed dipole moments. In 2D signals at short time delays, peaks merge into the central $\Omega=0$ peak, but the splitting is restored with increasing delay time t_2.

B. Dipole moment jumps between transversal and longitudinal orientations

We next turn to the second mechanism of exciton localization when perpendicular dipole moments do not couple (see Fig. 1). We now allow jumps between transverse [state $q_m=1$; $\vec{\boldsymbol{\mu}}_m=(\mu,0,0)$] and longitudinal [$q_m=-1$; $\vec{\boldsymbol{\mu}}_m=(0,\mu,0)$] orientation with respect to the aggregate axis

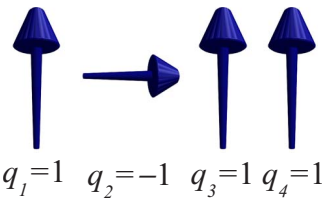

FIG. 8. Sample configuration of transition dipoles *uduu* of model in Sec. III B.

$\vec{d}_{mn}=D_0(0,m-n,0)$. Figure 8 shows an example configuration. We examine the tensor structure of response as measured by different pulse polarization configurations.[42–44]

The site frequencies [Eq. (21)] are

$$\varepsilon_m=\bar{\varepsilon}+\frac{\mu\mathcal{E}_m^x+\mu\mathcal{E}_m^y}{2}+\frac{\mu\mathcal{E}_m^x-\mu\mathcal{E}_m^y}{2}q_m.$$

We set $\bar{\varepsilon}_m+\mu(\mathcal{E}_m^x+\mathcal{E}_m^y)/2=0$ and denote $\varepsilon\equiv\mu(\mathcal{E}_m^x-\mathcal{E}_m^y)/2$ so that

$$\varepsilon_m=q_m\varepsilon. \tag{24}$$

Nearest neighbor intermolecular coupling [Eq. (19) and Fig. 1] can be recast in the form

$$J_{mm+1}=\frac{J}{4}[3(q_m+q_n)-(q_mq_n+1)]. \tag{25}$$

The interaction with the optical field is described by a Hamiltonian,

$$\hat{H}'_{\{q\}}=-\sum_{m=1}^{N}\sum_{j=1}^{3}\frac{\mu}{2}\{[q_m+1]E_j^x-[q_m-1]E_j^y\}\hat{B}_m^\dagger f(t-\tau_j)e^{i\vec{\mathbf{k}}_j\cdot\vec{r}-i\omega_j t}$$
$$-\sum_{m=1}^{N}\sum_{j=1}^{3}\frac{\mu}{2}\{[q_m+1]E_j^x-[q_m-1]E_j^y\}\hat{B}_m f(t-\tau_j)e^{-i\vec{\mathbf{k}}_j\cdot\vec{r}+i\omega_j t}. \tag{26}$$

The optical response is calculated by using Eqs. (11) and (12) after bosonization procedure Eqs. (14) and (15).

Oriented samples give 3^2 tensor components of the absorption spectra and up to 3^4 tensor components of the third order response. Two possible orientations (along x and y axes) of transition dipole in our model still allow 4 and 16 components for the linear and the third order responses, respectively.

For randomly oriented aggregates, there are few independent tensor structure components. The only isotropic component of linear response is $I=I^{xx}+I^{yy}$. There are three independent components of the isotropic third order response, which give three independent signals,[45]

$$\mathcal{R}^{(1)}(t_3,t_2,t_1)=\sum_{ab=x,y}R^{aabb}(t_3,t_2,t_1)$$
$$=R^{xxxx}+R^{yyyy}+R^{xxyy}+R^{yyxx},$$

$$\mathcal{R}^{(2)}(t_3,t_2,t_1)=\sum_{ab=x,y}R^{abba}(t_3,t_2,t_1)$$
$$=R^{xxxx}+R^{yyyy}+R^{xyyx}+R^{yxxy}, \tag{27}$$

$$\mathcal{R}^{(3)}(t_3,t_2,t_1)=\sum_{ab=x,y}R^{abab}(t_3,t_2,t_1)$$
$$=R^{xxxx}+R^{yyyy}+R^{xyxy}+R^{yxyx},$$

where R^{ijkl} are the response functions evaluated in the molecular frame. The averaged signal $\mathbf{R}^{abcd}$ in the real space can be calculated using the transformation[45]

$$\mathbf{R}^{abcd}=\frac{1}{30}(\delta_{ab}\delta_{cd},\quad\delta_{ad}\delta_{bc},\quad\delta_{ac}\delta_{bd})\begin{pmatrix}4&-1&-1\\-1&4&-1\\-1&-1&4\end{pmatrix}\times\begin{pmatrix}\mathcal{R}^{(1)}\\\mathcal{R}^{(2)}\\\mathcal{R}^{(3)}\end{pmatrix}.$$

In the slow bath limit we found that R^{xyyx}, R^{yxxy}, R^{xyxy}, and R^{yxyx} are much weaker than R^{xxxx}, R^{xxyy}, R^{yyxx}, and R^{yyyy}. The two signals $\mathcal{R}^{(2)}(t_3,t_2,t_1)\approx\mathcal{R}^{(3)}(t_3,t_2,t_1)$ are very similar and dominated by the R^{xxxx} and R^{yyyy} contributions. The system dynamics can be better extracted from combined signal $\mathcal{R}^{(3)}-\mathcal{R}^{(2)}=R^{xyxy}+R^{yxyx}-R^{xyyx}-R^{yxxy}$.

We start with the absorption spectra. Three independent tensor components of the linear responses I^{xx}, I^{yy}, and $I^{xy}=I^{yx}$ (cross components are the same due to Onsager reciprocity relation[46]) can be measured at oriented samples such as crystals. Figure 9 shows the I^{xx}, I^{yy}, and I^{xy} components of absorption for a slowly fluctuating tetramer. Peaks A′, B′, C′, and D′ (I^{xx} component) have same positions and magnitudes as in Fig. 3 and similarly represent d, dd, ddd, and $dddd$ clusters. Peak positions $\Delta\Omega\equiv\Omega+\varepsilon=0$ (peak A), $-2J$ (B), $-2\sqrt{2}J$ (C), and $-(1+\sqrt{5})J$ (D) of I^{yy} scales differently from Fig. 3 because the intermolecular coupling has factor of (-2) in $u\ldots u$ clusters (see Fig. 1).

In contrast to the model in Sec. III A, the peak structure remains similar to Fig. 9 even for $J\gg\varepsilon$ because the intermolecular coupling between perpendicular transition dipoles completely vanishes (see Fig. 1), and the model has no strong coupling limit. For the same reason, peaks are not

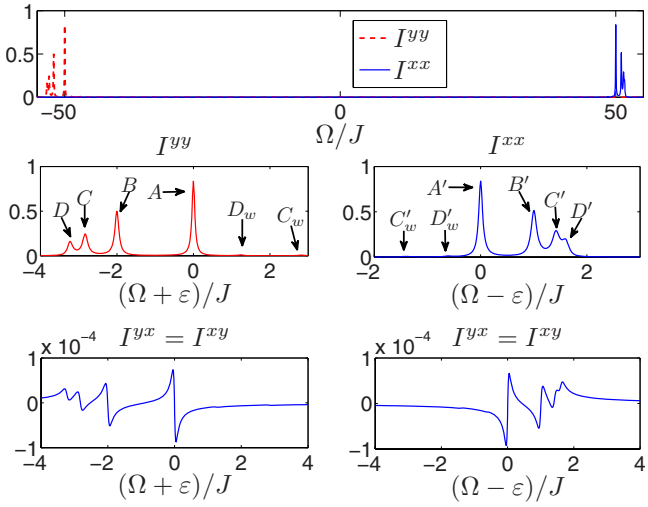

FIG. 9. Tensor components of the absorption spectrum [Im I(Ω), Eq. (11)] of a weakly coupled $J/\varepsilon=0.02$ tetramer [Eqs. (24) and (25) and Fig. 8] in the slow bath limit $k/J=0.02$. Top panel: averaged spectrum. Central panels: I^{xx} and I^{yy} components. Bottom panels: $I^{xy}=I^{yx}$ component.

further structured by cluster surrounding (contrast to bottom panel of Fig. 3), frequencies obtained by diagonalization of cluster Hamiltonian are exact.

The cross tensor component I^{xy} is weak (especially in the weak coupling limit) unless the bath jump rates become comparable with J,ε.

Next we turn to the 2D spectra. Figure 10 displays $-\mathrm{Im}\,\mathcal{R}^{(1)}_{\mathbf{k}_\mathrm{I}}(\Omega_3,t_2=0,-\Omega_1)$ in the slow bath limit. Since $x(y)$ polarized pulses excited primarily u-states (d- states) resonant around $\Omega\sim\varepsilon(\Omega\sim-\varepsilon)$, contributions R^{xxyy}, R^{xxxx}, R^{yyyy} and R^{yyxx} shows up in different regions $(\Omega_1,\Omega_3)\sim(-\varepsilon,\varepsilon)$, $\sim(\varepsilon,\varepsilon)$, $\sim(-\varepsilon,-\varepsilon)$, $\sim(\varepsilon,-\varepsilon)$ of 2D spectrum, respectively. Other contributions, e.g., R^{xxxx} in regions $(-\varepsilon,\varepsilon)$, $(-\varepsilon,-\varepsilon)$, and $(\varepsilon,-\varepsilon)$, are very weak. The diagonal peaks of R^{yyyy} and R^{xxxx} can be assigned to A–D and A′–D′ patterns of the absorption. Negative peaks correspond to excited state absorption. Their positions agree with Fig. 4 in the R^{xxxx} signal and reflect the reversed positions of A–D peaks (see Fig. 9) in R^{yyyy} signal.

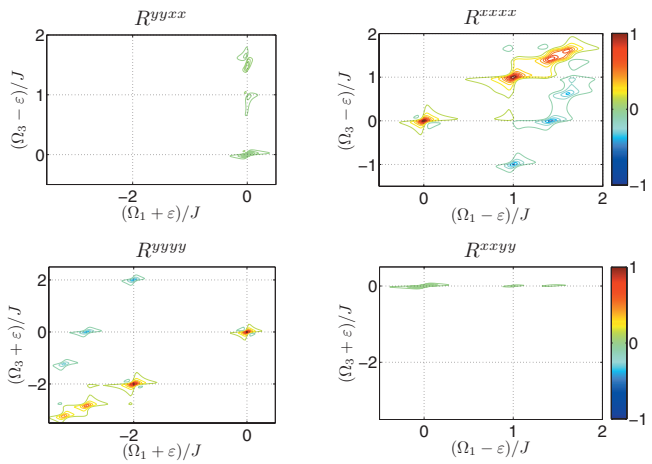

FIG. 10. $-\mathrm{Im}\,\mathcal{R}^{(1)}_{\mathbf{k}_\mathrm{I}}(\Omega_3,t_2,-\Omega_1)$ signal (27) for tetramer (Fig. 8) at zero delay times $t_2=0$. Molecular tensor components show up in different regions of 2D spectra as marked. Parameters: $J/\varepsilon=0.02$ and $k=0.02J$.

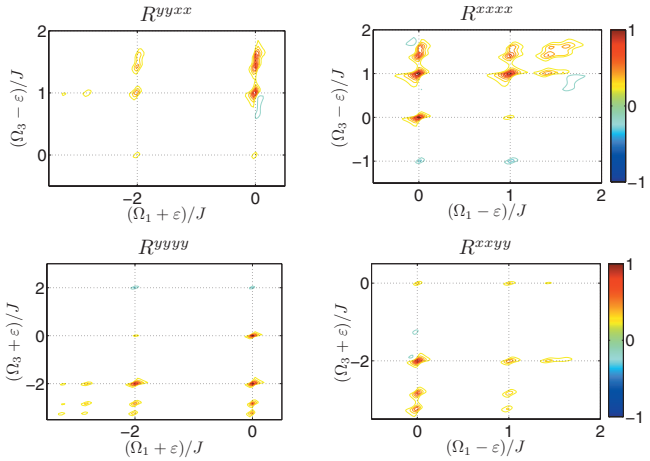

FIG. 11. Same signal and system as in Fig. 10 but at longer delay time $kt_2=1$.

The R^{xxyy} and R^{yyxx} signals (antidiagonal regions in Fig. 10) are much weaker at short delay times because the signal [see Eq. (12)] is linear in the diagonal two exciton coupling V [in the exciton index; see Eq. (14)]. For static bath each exciton is connected with fixed orientation of transition dipole moment, and the $R^{xxyy}(R^{yyxx})$ contribution only shows up with $u\leftrightarrow d$ jumps during t_2 interval. This insight is typical for the NEE description. In the SLE approach, elimination of most contributions of two static, noncoupled clusters is due to destructive interference between various LSPs, and the spectra are thus harder to interpret.[2]

As the delay time is varied (Fig. 11), the $\mathcal{R}^{(1)}_{\mathbf{k}_\mathrm{I}}$ signal acquires various cross peaks, which reflect the dynamics of cluster transformation. Peak pattern is similar to Fig. 5 (except the reversal positions of A–D peaks) since the bath model [Eq. (16)] was not changed.

The other $-\mathrm{Im}[\mathcal{R}^{(3)}_{\mathbf{k}_\mathrm{I}}(\Omega_3,t_2=0,-\Omega_1)-\mathcal{R}^{(2)}_{\mathbf{k}_\mathrm{I}}(\Omega_3,t_2=0,-\Omega_1)]$ signal plotted in Fig. 12 is also weak since it requires jumps during t_1 and/or t_3 intervals and disappears in static $k=0$ limit. The mixed tensor components R^{xyxy}, R^{yxyx} R^{xyyx},

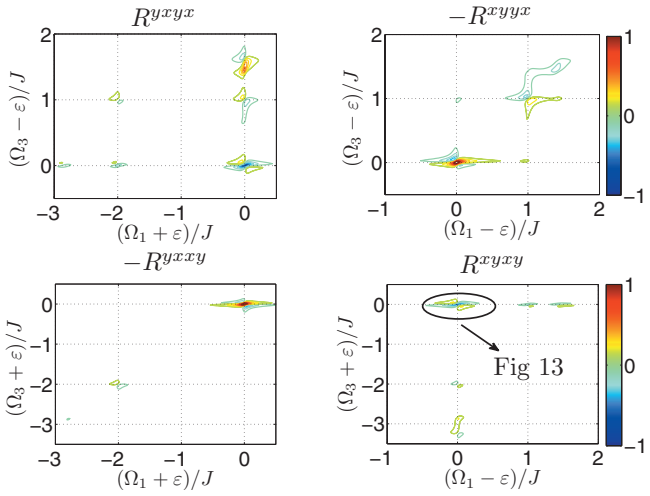

FIG. 12. $-\mathrm{Im}[\mathcal{R}^{(3)}_{\mathbf{k}_\mathrm{I}}(\Omega_3,t_2,-\Omega_1)-\mathcal{R}^{(2)}_{\mathbf{k}_\mathrm{I}}(\Omega_3,t_2,-\Omega_1)]$ signal (27) for tetramer (Fig. 8) at zero delay time $t_2=0$. Parameters $J/\varepsilon=0.02$ and $k/J=0.02$ correspond to Figs. 10 and 11. Molecular tensor components show up in different regions of 2D spectra as marked.

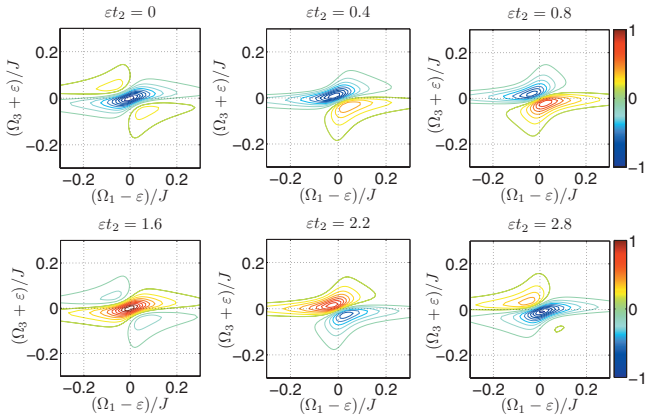

FIG. 13. Intensity oscillations at the peak marked at Fig. 12 at short delay times: top (from left): εt_2=0, 0.4, and 0.8; bottom (from left): εt_2=1.6, 2.2, and 2.8.

and R^{yxxy} show up in various regions of the 2D spectra. Since different parts of the aggregate are excited by the first and by the second pulse, the system is evolving in the coherence during the second interval and the peaks shows (Fig. 13) short time oscillations of the period π/ε. At longer $t_2 \approx 1/k$ delay times rich cross peak structure is build (Fig. 14) as bath jumps transform the clusters.

IV. DISCUSSION

Starting with a stochastic Hamiltonian model of fluctuations recast in the quasiparticle representation, we derived a set of SNEEs and used them to simulate the nonlinear response of a model tetramer whose chromophores undergo two types of orientation fluctuations. Flipping between two transverse orientations disentangles molecules when associated frequency shift is larger than coupling (weak coupling limit). Swinging between transverse and longitudinal orientations reduces the delocalization length because perpendicular transition dipoles do not couple. Clusters of parallel molecules act cooperatively in Dicke-type quantum process and dominate the spectra of even randomly switching molecules without any dynamical bias of oriented structures. Signatures of the length of ordered domain are seen in spectrum. The variation in 2D spectra with delay time thus provides direct view into the structural transformation of aggregate. Cross peaks were uniquely associated with specific transformation of clusters. Rates of transformation can be estimated by measuring cross peak volumes.

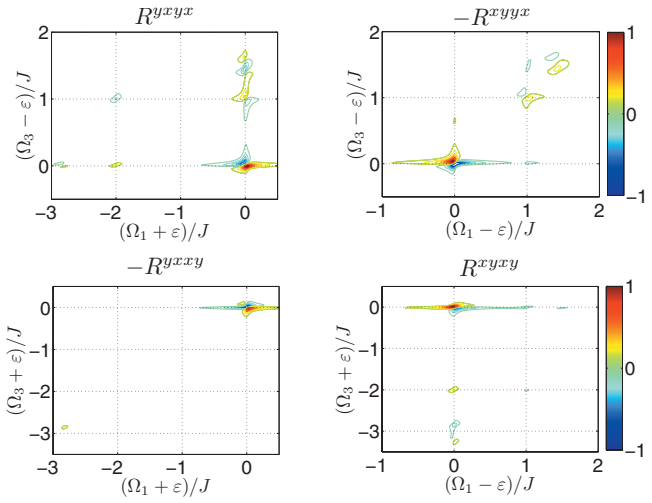

FIG. 14. Same signal as in Fig. 12 but at long delay time kt_2=0.8.

The present formalism can be applied to any type of Markovian orientation dynamics. For instance, the orientational ordering of, e.g., water molecules in carbon nanotubes,[28] may be straightforwardly included by finite temperature generalization of the rate matrix [Eqs. (17) and (18)], which represents the ground state dipole-dipole interaction.

The present simulations used the complete SNEE, which exactly represent quantum stochastic dynamics (equivalently to full SLE). Once approximations are made, the SLE and SNEE are not equivalent. To save cost NEE implementations often factorize double (triple) exciton averages into products of lower ones. This natural approximation for the NEE cannot be easily made in the SLE. The stochastic fluctuations build statistical correlations between variables, which are different from that of quantum ones neglected in the NEE. Straightforward factorization strategy also may not lead to effective cost reduction since these are often based on Hilbert space diagonalization, which is not possible for the SNEE. The development of effective and accurate approximate schemes for the SNEE approach constitutes a challenge for the future.

ACKNOWLEDGMENTS

The support of the Grant Agency of the Czech Republic (Grant No. 202/07/P245), the Ministry of Education of the Czech Republic (Research Program No. MSM 0021620835), the National Science Foundation (Grant No. CHE-0745892), and the National Institutes of Health (Grant No. GM59230) is gratefully acknowledged.

APPENDIX A: AVERAGING OVER BATH PATHS

Individual trajectories of the bath process $\{q\}(t)$ and the observable $A(\{q\}(t))$ are not traced in bulk measurements. Instead, observable ensemble averages are calculated by applying probability measure $\mathcal{D}\{q\}(t)$ on sigma algebra of trajectories $\{q\}(t)$.

The path integration can be carried out exactly for Markovian processes in two ways. In the first we start from the SLEs,[10,11]

$$\frac{d\hat{\rho}_{\{q\}}(t)}{dt} = \frac{-i}{\hbar}[\hat{H}(\{q\}) + \hat{H}'(\{q\},t), \hat{\rho}_{\{q\}}] + \sum_{\{q'\}} T_{\{q\}\{q'\}}\hat{\rho}_{\{q'\}}. \tag{A1}$$

Equations of motions for averages $\langle\hat{A}\rangle_{\{q\}} = \mathrm{Tr}\hat{A}\hat{\rho}_{\{q'\}}$ for any operator $\hat{A} = \hat{b}_m, \hat{b}_m\hat{b}_n, \hat{b}_m^\dagger\hat{b}_n, \ldots$ can be calculated by applying SLE [Eq. (A1)] to $(d/dt)\langle A\rangle_{\{q\}}$. This results in the SNEE

$$\frac{d\langle A\rangle_{\{q\}}(t)}{dt} = \frac{i}{\hbar}\langle[\hat{H}+\hat{H}'(t),A]\rangle_{\{q\}} + \sum_{\{q'\}} T_{\{q\}\{q'\}}\langle A\rangle_{\{q'\}}. \tag{A2}$$

This approach employs that the path integration was already made when deriving SLEs.[11]

In an alternative approach, the solution to NEEs of a general form

$$\frac{dA_i}{dt} = \sum_j C_{ij}(\{q\}(t))A_j(t) + g_i(\{q\}(t),t) \tag{A3}$$

can be averaged over bath paths $\langle A_i\rangle = \int A_i(\{q\}(t))\mathcal{D}\{q\}(t)$, resulting in the path integral

$$\langle A_i\rangle(t) = \int \mathcal{D}\{q\}(t)\left\{\exp_+\left[\int_0^t \sum_j C_{ij}(\{q\}(t'))dt'\right] + \int dt' \exp_+\left[\int_{t'}^t \sum_j C_{ij}(\{q\}(t''))dt''\right] g_i(\{q\}(t'),t')\right\}.$$

By carrying out the path integration for a Markovian process, we obtain

$$\langle A_i\rangle(t) = \int d\{q\}(t)d\{q\}(0)P(\{q\}(0)) \times\left\{\left[\exp_+\left[\left(\sum_j C_{ij}(\{q\}) + T(\{q\})\right)t\right]\right]_{\{q\}(t),\{q\}(0)} + \left[\int_0^t dt' \exp_+\left[\left(\sum_j C_{ij}(\{q\}) + \hat{T}(\{q\})\right)(t-t')\right] \times g_i(\{q\},t')\right]_{\{q\}(t),\{q\}(0)}\right\}.$$

An integration over the initial and final states $\langle A_i\rangle(t) = \Sigma_{\{q\}(0),\{q\}(t)}P(\{q\}(0))A_i(\{q\},t)$ of the solution $A_i'(\{q\}(t),\{q\}(0),t)$ to the stochastic nonlinear equations is required,

$$\frac{\partial A_i'(\{q\},t)}{dt} = \sum_j C_{ij}(\{q\})A_j'(\{q\},t) + g_i(\{q\},t) + \sum_{\{q\}'} T_{\{q\}\{q\}'}A_i'(\{q\}',t). \tag{A4}$$

APPENDIX B: SURVEY OF THIRD ORDER SIGNALS

The SNEE [Eqs. (4)–(7)] can be used to calculate third order response. The macroscopic signal integrated over the sample is proportional to

$$S^a_{\vec{\mathbf{k}}} = \frac{1}{(2\pi)^3}\int d^3r e^{-i\vec{\mathbf{k}}\cdot\vec{r}}\mathbf{P}^a(t_1+t_2+t_3,\vec{r}) = \frac{1}{(2\pi)^3}\int d^3r e^{-i\vec{\mathbf{k}}\cdot\vec{r}}\sum_m\sum_{\{q\}}\boldsymbol{\mu}^a_{m;\{q\}}\langle b_m\rangle_{\{q\}}(t_1+t_2+t_3,\vec{r}).$$

We have to isolate the third order contribution. After bit of algebra we limit signal to six possible phase matching directions proportional to three independent response functions,

$$\begin{aligned} S^a_{\vec{\mathbf{k}}}(t_3,t_2,t_1) = {} & \delta(\vec{\mathbf{k}}+\vec{\mathbf{k}}_1-\vec{\mathbf{k}}_2-\vec{\mathbf{k}}_3)\sum_{bcd} R^{abcd}_{\mathbf{k}_\mathrm{I}}(t_3,t_2,t_1)E^b_3E^c_2E^d_1 \\ & + \delta(\vec{\mathbf{k}}-\vec{\mathbf{k}}_1+\vec{\mathbf{k}}_2-\vec{\mathbf{k}}_3)\sum_{bcd} R^{abcd}_{\mathbf{k}_\mathrm{II}}(t_3,t_2,t_1)E^b_3E^c_2E^d_1 \\ & + \delta(\vec{\mathbf{k}}-\vec{\mathbf{k}}_1-\vec{\mathbf{k}}_2+\vec{\mathbf{k}}_3)\sum_{bcd} R^{abcd}_{\mathbf{k}_\mathrm{III}}(t_3,t_2,t_1)E^b_3E^c_2E^d_1 \\ & + \delta(\vec{\mathbf{k}}-\vec{\mathbf{k}}_1+\vec{\mathbf{k}}_2+\vec{\mathbf{k}}_3)\sum_{bcd} R^{abcd*}_{\mathbf{k}_\mathrm{I}}(t_3,t_2,t_1)E^b_3E^c_2E^d_1 \\ & + \delta(\vec{\mathbf{k}}+\vec{\mathbf{k}}_1-\vec{\mathbf{k}}_2+\vec{\mathbf{k}}_3)\sum_{bcd} R^{abcd*}_{\mathbf{k}_\mathrm{II}}(t_3,t_2,t_1)E^b_3E^c_2E^d_1 \\ & + \delta(\vec{\mathbf{k}}+\vec{\mathbf{k}}_1+\vec{\mathbf{k}}_2-\vec{\mathbf{k}}_3)\sum_{bcd} R^{abcd*}_{\mathbf{k}_\mathrm{III}}(t_3,t_2,t_1)E^b_3E^c_2E^d_1. \end{aligned} \tag{B1}$$

In Eq. (B1) we have denoted the time intervals $t_1=\tau_2-\tau_1$, $t_2=\tau_3-\tau_2$, and $t_3=t-\tau_3$. Signal in $\vec{\mathbf{k}}_\mathrm{I}=-\vec{\mathbf{k}}_1+\vec{\mathbf{k}}_2+\vec{\mathbf{k}}_3$ phase matching direction is

$$\begin{aligned} R^{abcd}_{\mathbf{k}_\mathrm{I}}(t_3,t_2,t_1) = {} & 2i\sum_{m_{1-4}m'_{1-4}m''_{1-2}m'''_1}\sum_{q^{\alpha-\eta}}\left(\frac{i}{\hbar}\right)^3 \\ & \times\boldsymbol{\mu}^{a*}_{m_4;\{q^\delta\}}\boldsymbol{\mu}^{b}_{m_3;\{q^\gamma\}}\boldsymbol{\mu}^{c}_{m_2;\{q^\beta\}}\boldsymbol{\mu}^{d*}_{m_1;\{q^\alpha\}} \\ & \times\int_0^{t_3} dt' G_{m_4\{q^\delta\}m'_4\{q^\eta\}}(t')V_{m'_4m'_1,m'_3m'_2;\{q^\eta\}} \\ & \times\mathcal{G}^{(Z)}_{m'_1m'_3m'_2\{q^\eta\},m''_1m_3m''_2\{q^\gamma\}}(t_3-t') \\ & \times\mathcal{G}^{(N)}_{m''_1m''_2\{q^\gamma\},m'''_1m_2\{q^\beta\}}(t_2) \\ & \times G^*_{m'''_1\{q^\beta\},m_1\{q^\alpha\}}(t_1)P(\{q^\alpha\}). \end{aligned} \tag{B2}$$

The dt' convolution can be effectively carried out in the frequency domain

$$R^{abcd}_{\mathbf{k}_\mathrm{I}}(\Omega_3,\Omega_2,\Omega_1) = \int_0^\infty dt_1\int_0^\infty dt_2\int_0^\infty dt_3 e^{i(\Omega_1t_1+\Omega_2t_2+\Omega_3t_3)} \times R^{abcd}_{\mathbf{k}_\mathrm{I}}(t_3,t_2,t_1), \tag{B3}$$

resulting in Eqs. (12). This *photon echo* signal is simulated in the figures.

Third order signals in others phase matching directions $\vec{\mathbf{k}}_\mathrm{II}=\vec{\mathbf{k}}_1-\vec{\mathbf{k}}_2+\vec{\mathbf{k}}_3$ and $\vec{\mathbf{k}}_\mathrm{III}=\vec{\mathbf{k}}_1+\vec{\mathbf{k}}_2-\vec{\mathbf{k}}_3$ are obtained as

$$R^{abcd}_{\mathbf{k}_{\mathrm{II}}}(t_3,t_2,t_1) = 2i \sum_{m_{1-4}m'_{1-4}m''_{1-2}m'''_1} \sum_{q^{\alpha-\eta}} \left(\frac{i}{\hbar}\right)^3 \times \boldsymbol{\mu}^{a*}_{m_4;\{q^\delta\}} \boldsymbol{\mu}^{b}_{m_3;\{q^\gamma\}} \boldsymbol{\mu}^{c*}_{m_2;\{q^\beta\}} \boldsymbol{\mu}^{d}_{m_1;\{q^\alpha\}} \times \int_0^{t_3} dt' G_{m_4\{q^\delta\}m'_4\{q^\eta\}}(t') V_{m'_4m'_2,m'_3m'_1;\{q^\eta\}} \times \mathcal{G}^{(Z)}_{m'_2m'_3m'_1\{q^\eta\},m''_2m_3m''_1\{q^\gamma\}}(t_3-t') \times \mathcal{G}^{(N)}_{m''_2m''_1\{q^\gamma\},m_2m'''_1\{q^\beta\}}(t_2) \times G_{m'''_1\{q^\beta\}m_1\{q^\alpha\}}(t_1) P(\{q^\alpha\}) \quad \text{(B4)}$$

and

$$R^{abcd}_{\mathbf{k}_{\mathrm{III}}}(t_3,t_2,t_1) = 2i \sum_{m_{1-4}m'_{1-4}m''_{1-2}m'''_1} \sum_{q^{\alpha-\eta}} \left(\frac{i}{\hbar}\right)^3 \times \boldsymbol{\mu}^{a*}_{m_4;\{q^\delta\}} \boldsymbol{\mu}^{b*}_{m_3;\{q^\gamma\}} \boldsymbol{\mu}^{c}_{m_2;\{q^\beta\}} \boldsymbol{\mu}^{d}_{m_1;\{q^\alpha\}} \times \int_0^{t_3} dt G_{m_4\{q^\delta\}m'_4\{q^\eta\}}(t') V_{m'_4m'_3,m'_2m'_1;\{q^\eta\}} \times \mathcal{G}^{(Z)}_{m'_3m'_2m'_1\{q^\eta\},m_3m''_2m''_1\{q^\gamma\}}(t_3-t') \times \mathcal{G}_{m''_2m''_1\{q^\gamma\},m_2m'''_1\{q^\beta\}}(t_2) \times G_{m'''_1\{q^\beta\}m_1\{q^\alpha\}}(t_1) P(\{q^\alpha\}), \quad \text{(B5)}$$

respectively. Equations (B4) and (B5) can be transformed to Fourier domain along the same lines as Eq. (B2), yielding

$$R^{abcd}_{\mathbf{k}_{\mathrm{II}}}(\Omega_3,\Omega_2,\Omega_1) = 2i \sum_{m_{1-4}m'_{1-4}m''_{1-2}m'''_1} \sum_{q^{\alpha-\eta}} \left(\frac{i}{\hbar}\right)^3 \times \boldsymbol{\mu}^{a*}_{m_4;\{q^\delta\}} \boldsymbol{\mu}^{b}_{m_3;\{q^\gamma\}} \boldsymbol{\mu}^{c*}_{m_2;\{q^\beta\}} \boldsymbol{\mu}^{d}_{m_1;\{q^\alpha\}} \times G_{m_4\{q^\delta\}m'_4\{q^\eta\}}(\Omega_3) V_{m'_4m'_2,m'_3m'_1;\{q^\eta\}} \times \mathcal{G}^{(Z)}_{m'_2m'_3m'_1\{q^\eta\},m''_2m_3m''_1\{q^\gamma\}}(\Omega_3) \times \mathcal{G}^{(N)}_{m''_2m''_1\{q^\gamma\},m_2m'''_1\{q^\beta\}}(\Omega_2) \times G_{m'''_1\{q^\beta\}m_1\{q^\alpha\}}(\Omega_1) P(\{q^\alpha\}), \quad \text{(B6)}$$

$$R^{abcd}_{\mathbf{k}_{\mathrm{III}}}(\Omega_3,\Omega_2,\Omega_1) = 2i \sum_{m_{1-4}m'_{1-4}m''_{1-2}m'''_1} \sum_{q^{\alpha-\eta}} \left(\frac{i}{\hbar}\right)^3 \times \boldsymbol{\mu}^{a*}_{m_4;\{q^\delta\}} \boldsymbol{\mu}^{b*}_{m_3;\{q^\gamma\}} \boldsymbol{\mu}^{c}_{m_2;\{q^\beta\}} \boldsymbol{\mu}^{d}_{m_1;\{q^\alpha\}} \times G_{m_4\{q^\delta\}m'_4\{q^\eta\}}(\Omega_3) V_{m'_4m'_3,m'_2m'_1;\{q^\eta\}} \times \mathcal{G}^{(Z)}_{m'_3m'_2m'_1\{q^\eta\},m_3m''_2m''_1\{q^\gamma\}}(\Omega_3) \times \mathcal{G}_{m''_2m''_1\{q^\gamma\},m_2m'''_1\{q^\beta\}}(\Omega_2) \times G_{m'''_1\{q^\beta\}m_1\{q^\alpha\}}(\Omega_1) P(\{q^\alpha\}). \quad \text{(B7)}$$

Equations (12) and (B2)–(B7) provide an exact representation of the nonlinear response for stochastic Frenkel Hamiltonian model of aggregate.

[1] S. Mukamel, *Principles of Nonlinear Optical Spectroscopy* (Oxford University Press, New York, 1995).
[2] D. Abramavicius, B. Palmieri, D. V. Voronine, F. Šanda, and S. Mukamel, Chem. Rev. (Washington, D.C.) **109**, 2350 (2009).
[3] M. Cho, *Two-Dimensional Optical Spectroscopy* (CRC, Boca Raton, 2009).
[4] V. May and O. Kühn, *Charge and Energy Transfer Dynamics in Molecular Systems: A Theoretical Introduction* (Wiley-VCH, Weinheim, 2000).
[5] P. L. McRobbie, G. Hanna, Q. Shi, and E. Geva, Acc. Chem. Res. **42**, 1299 (2009).
[6] M. Cho, Chem. Rev. (Washington, D.C.) **108**, 1331 (2008).
[7] A. G. Redfield, Adv. Magn. Reson. **1**, 1 (1965).
[8] V. Chernyak and S. Mukamel, J. Chem. Phys. **105**, 4565 (1996).
[9] R. Kubo, J. Math. Phys. **4**, 174 (1963).
[10] D. Gamliel and H. Levanon, *Stochastic Processes in Magnetic Resonance* (World Scientific, Singapore, 1995).
[11] Y. Tanimura, J. Phys. Soc. Jpn. **75**, 082001 (2006).
[12] A. Garg, J. N. Onuchic, and V. Ambegaokar, J. Chem. Phys. **83**, 4491 (1985).
[13] A. Ishizaki and Y. Tanimura, J. Chem. Phys. **125**, 084501 (2006).
[14] A. Ishizaki and G. R. Fleming, Proc. Natl. Acad. Sci. U.S.A. **106**, 17255 (2009).
[15] T. C. Jansen and J. Knoester, Acc. Chem. Res. **42**, 1405 (2009).
[16] C. Falvo, B. Palmieri, and S. Mukamel, J. Chem. Phys. **130**, 184501 (2009).
[17] A. Paarmann, T. Hayashi, S. Mukamel, and R. J. D. Miller, J. Chem. Phys. **128**, 191103 (2008).
[18] J. Seehusen, D. Schwarzer, J. Lindner, and P. Vöhringer, Phys. Chem. Chem. Phys. **11**, 8484 (2009).
[19] J. Zheng, K. Kwak, J. Asbury, X. Chen, I. R. Piletic, and M. D. Fayer, Science **309**, 1338 (2005).
[20] F. Šanda and S. Mukamel, J. Chem. Phys. **125**, 014507 (2006).
[21] M. D. Fayer, D. E. Moilanen, D. Wong, D. E. Rosenfeld, E. E. Fenn, and S. Park, Acc. Chem. Res. **42**, 1210 (2009).
[22] R. R. Ernst, G. Bodenhausen, and A. Wokaun, *Principles of Nuclear Magnetic Resonance in One and Two Dimensions* (Oxford University Press, New York, 1987).
[23] F. Šanda and S. Mukamel, Phys. Rev. Lett. **98**, 080603 (2007).
[24] F. Šanda and S. Mukamel, J. Phys. Chem. B **112**, 14212 (2008).
[25] T. C. Jansen, W. Zhuang, and S. Mukamel, J. Chem. Phys. **121**, 10577 (2004).
[26] S. Mukamel, in *Molecular Nonlinear Optics*, edited by J. Zyss (Academic, New York, 1994), pp. 1–46.
[27] V. Chernyak, W. M. Zhang, and S. Mukamel, J. Chem. Phys. **109**, 9587 (1998).
[28] J. Kofinger, G. Hummer, and C. Dellago, Proc. Natl. Acad. Sci. U.S.A. **105**, 13218 (2008).
[29] D. Laage, G. Stirnemann, and J. T. Hynes, J. Phys. Chem. B **113**, 2428 (2009).
[30] D. Laage and J. T. Hynes, Science **311**, 832 (2006).
[31] R. Rey, K. Møller, and J. T. Hynes, J. Phys. Chem. A **106**, 11993 (2002).
[32] J. Janusonis, L. Valkunas, D. Rutkauskas, and R. van Grondelle, Biophys. J. **94**, 1348 (2008).
[33] L. Valkunas, J. Janusonis, D. Rutkauskas, and R. van Grondelle, J. Lumin. **127**, 269 (2007).
[34] N. G. van Kampen, *Stochastic Processes in Physics and Chemistry* (North-Holland, Amsterdam, 1992).
[35] F. Šanda and S. Mukamel, J. Chem. Phys. **124**, 124103 (2006).
[36] A. S. Davydov, *Theory of Molecular Excitons* (McGraw-Hill, New York, 1962).
[37] E. A. Silinsh and V. Čápek, *Organic Molecular Crystals: Interaction, Localization and Transport Phenomena* (AIP, New York, 1994).
[38] H. van Amerongen, L. Valkunas, and R. van Grondelle, *Photosyntetic Excitons* (World Scientific, Singapore, 2000).
[39] M. Combescot, O. Betbeder-Matibet, and F. Dubin, Phys. Rep. **463**, 215 (2008).
[40] R. Kubo, in *Fluctuation, Relaxation and Resonance in Magnetic Systems*, edited by D. ter Haar (Oliver and Boyd, Edinburgh, 1962), p. 23.

[41] P. W. Anderson, J. Phys. Soc. Jpn. **9**, 316 (1954).
[42] M. T. Zanni, N. H. Ge, Y. S. Kim, and R. M. Hochstrasser, Proc. Natl. Acad. Sci. U.S.A. **98**, 11265 (2001).
[43] S. Woutersen and P. Hamm, J. Phys. Chem. B **104**, 11316 (2000).
[44] K. J. Kubarych, C. J. Milne, S. Lin, V. Astinov, and R. J. D. Miller, J. Chem. Phys. **116**, 2016 (2002).
[45] D. L. Andrews and T. Thirunamachandran, J. Chem. Phys. **67**, 5026 (1977).
[46] E. Fick and G. Sauermann, *The Quantum Statistics of Dynamic Processes* (Springer, Berlin, 1990).